Tropospheric Atmospheric Heterogeneities of ALOS-2 Interferograms in the Greater Bay Area

Peng Liu and Xiaofei Chen

***Abstract*—*L*-band advanced land observing satellite-2 (ALOS-2) images are a good source of radar data with better coherence than *C*-band images. However, significant ionospheric effects are often associated with *L*-band interferograms. In addition, the tropospheric delay can also be severe in subtropical coastal environments. In this work, different methods are adopted, adapted, or proposed to evaluate the tropospheric signals in ALOS-2 interferograms in the Shenzhen region. Ionospheric effects are estimated by the split spectrum method. Tropospheric delays are estimated through their height dependence or numerical weather prediction models. In addition to the conventional weighting methods that consider distance, variation, and Gaussian models, a stepwise approach to estimate tropospheric signals from height or to scale numerical weather models is proposed in this study. A combination of spectrometer observation and air mass trajectories is also proposed to assess topography-independent tropospheric signals, specifically the moderate resolution imaging spectroradiometer (MODIS) water vapor fields and the Hybrid Single-Particle Lagrangian Integrated Trajectory model. Meanwhile, possible cloud and wind patterns are observed from interferogram. This work demonstrates the feasibility of stepwise estimation of stratified signals using height information or numerical weather models. It also shows the potential for air mass trajectories to move water vapor fields to mitigate the influence of time difference between SAR and spectrometer acquisition times.**

***Index Terms*—Hybrid Single-Particle Lagrangian Integrated Trajectory (HYSPLIT) air mass trajectory, InSAR atmospheric effects, InSAR stratified delay, MODIS water vapor, numerical weather prediction (NWP) model, topography-independent tropospheric delay.**

I. Introduction

IONOSPHERIC effects and tropospheric effects are observed in repeat pass radar interferometry synthetic aperture radar (InSAR) and are major components of atmospheric phase screen (APS). Ionospheric effects are due to ionospheric heterogeneities at image acquisitions [1]. The free electron density in ionosphere varies with the activity of the Sun, the earth magnetic field, and the atmospheric parameters [2], [3], [4]. The ionospheric phase change across the interferogram is related to the total electron content difference between two SAR acquisitions. Ionospheric effects are frequency dispersive and have a greater impact on *L*-band interferograms than on shorter wavelength *C*- or *X*-band interferograms [5], [6]. Various ionospheric estimation methods are developed to remove ionospheric effects from the interferogram, including range split spectrum [6], range group delay [7], azimuth shift [8], and Faraday rotation [9] methods. This work uses a split spectrum approach to correct for ionospheric effects. The split spectrum method synthesizes two subband interferograms with different central frequencies at high and low bands. The ionospheric effects are estimated by cancelling nondispersive phase components through a combination of subband interferograms and frequencies [10] .

Tropospheric variations, such as water vapor, pressure, and temperature, together contribute to the tropospheric atmospheric heterogeneities of interferograms. Tropospheric distortion is independent of frequency but is dominant error in wet regions for *C*- and *X*-band interferometric products [11] and, therefore, another major error in *L*-band interferogram besides ionospheric effects.

InSAR time-series processing can be used to mitigate tropospheric atmospheric components [12], including stacking [13], spatiotemporal filtering, stochastic model [14], [15], interferogram selection [16], and deep learning methods [17]. Atmospheric filtering can be used to separate tropospheric signals from deformation through a combination of temporal high-pass and spatial low-pass filtering [18] if a sufficient number of images are available. Tropospheric effects are characterized by stratified signals and turbulent signals based on the empirical mathematical model (i.e., topography-correlated models), which are not deterministic as turbulent signals are highly variable in both spatial and temporal dimensions [19]. Stratified signals can be estimated from its height dependence by empirical methods with linear and power law relationship assumptions between stratified tropospheric delay and height [20], [21]. The residual components after removing the stratified signals are usually considered to be turbulent signals.

In addition to empirical models and InSAR time-series algorithms, external datasets can also be used to estimate tropospheric delay [22], [23], [24], [25]. Tropospheric signals can be deterministically divided into the wet delay and the hydrostatic delay. Although the hydrostatic delay is usually greater than the wet delay, the wet delay changes are greater than the hydrostatic delay changes for the interferogram by one order of magnitude [26]. Generally, spectrometer measurements can only be used to capture wet delay changes [27], while global navigation satellite

Manuscript received 18 March 2024; revised 6 May 2024; accepted 11 June 2024. Date of publication 13 June 2024; date of current version 1 July 2024. This work was supported in part by the National Natural Science Foundation of China Programs under Grant 42274036, in part by Shenzhen Science and Technology Programs under Grant JCYJ20220530112812029, in part by the Guangdong Provincial Key Laboratory of Geophysical High-resolution Imaging Technology under Grant 2022B1212010002, and in part by the open fund of the State Key Laboratory of Geodesy and Earth's Dynamics under Grant SKLGED2021-5-1. *(Corresponding author: Peng Liu.)*

The authors are with the Guangdong Provincial Key Laboratory of Geophysical High-Resolution Imaging Technology and the Department of Earth and Space Sciences, Southern University of Science and Technology, Shenzhen 518055, China (e-mail: liup3@sustech.edu.cn; chenxf@sustech.edu.cn).

Digital Object Identifier 10.1109/JSTARS.2024.3414111

system (GNSS) measurements [28] and numerical weather prediction (NWP) models can be used to obtain both the wet delay changes and hydrostatic delay changes [29]. Theoretically, NWP models provide the total delay, including both the stratified and turbulent signals, although the small-scale delays are hard to reconstruct due to the coarse resolution. Hence, tropospheric estimation from NWP models is mostly topography dependent.

Both the topography-dependent (TD) APS from the empirical model and the tropospheric estimates from the NWP model require scaling before correction. Spatial segmentation methods, such as regular grids [21] and irregular quadtree blocks generated from topography gradients [30], can be used to locally estimate the relationship between phase and height [30] or locally scale the relationship between phase and NWP predictions [21], to better accommodate variable phase–height or variable phase–NWP relationships in different regions within a single interferogram. However, it should also be noted that fine segmentation may overfit turbulence, while coarse segmentation may not be able to model the spatial variation of atmospheric delays [31]. Weighting methods [21], [32] or adaptively segmentation methods [31] can improve the performance of local window estimation. Alternatively, in this work, a stepwise estimation approach (SWEA) for variable phase–height or variable phase–NWP relationships is proposed for stratified tropospheric delay to mitigate overfitting of turbulence.

However, it should also be noted that when topography-independent APS dominates the InSAR atmospheric effects, the empirical model or NWP model correction may fail, especially for the subtropical coastal areas. Therefore, this work also aims to assess the InSAR atmospheric effects in this region when empirical models or NWP models exhibit different APS patterns from the interferograms.

Spectrometer observations can provide insights into both stratified and topography-independent signals. However, Li et al. [33] pointed out that the time difference between moderate resolution imaging spectroradiometer (MODIS) and SAR may be a limitation to their integrated approach. Atmospheric advection or convection in subtropical coastal environments is expected to cause rapid changes in water vapor. The spectrometer observation and InSAR water vapor field maybe misaligned as time difference exist between SAR and spectrometer observation times and water vapor field has changed during that period. For such reasons, this article also proposes to use air mass trajectories to improve the timeliness of spectrometer observations.

Trajectories are considered when correcting InSAR APS using GNSS observations. Onn and Zebker [34] used frozen flow hypothesis [35] to obtain a denser network of GNSS-derived wet delay for InSAR APS correction. The wind speed and direction are acquired from GPS-derived zenith wet delay (ZWD) time series to implement this hypothesis. Chang and He [36] also used the frozen flow hypothesis for InSAR APS correction with GNSS wet delay, but with the difference that mean wind is extracted from national centers for environmental prediction final (NCEP FNL). There exists another model named Hybrid Single-Particle Lagrangian Integrated Trajectory (HYSPLIT) [37], [38], developed by the Air Resources Laboratory of National Oceanic and Atmospheric Administration (NOAA). HYSPLIT has been used to track atmospheric aerosol patterns such as industrial emissions [39], dust storm [40], and volcanic ashes [41], among others. Air mass trajectories may help mitigate the mismatch between SAR and MODIS by their time difference.

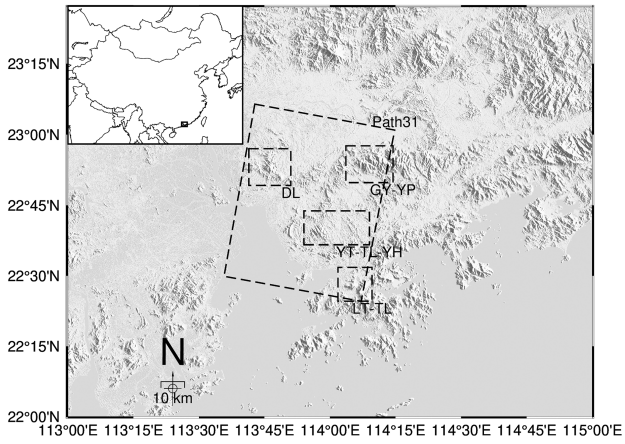

Fig. 1. Study area. The figure outlines the InSAR frame, DaLing (DL) hill, GuanYin-YinPing (GY-YP) hills, YangTai-TangLang-YinHu (YT-TL-YH) hills, and LamTsuen-TaiLam (LT-TL) Hills.

In this article, we use the split spectrum method to estimate ionospheric signals. For stratified signals, in addition to the existing spatial segmentation and weighting methods, we propose to estimate them using an SWEA for stratified tropospheric delay in height intervals and a stepwise scaling approach for NWP delays. For interferograms dominated by topography-independent tropospheric effects, we use MODIS near-infrared (IR) water vapor fields for correction. MODIS water vapor fields without obvious changes before and after SAR acquisition are used. We propose to consider the air mass trajectories of HYSPLIT to reduce the effect of the time difference between MODIS and SAR acquisition times.

II. Data and Methods

A. SAR Data

The *L*-band advanced land observing satellite-2 (ALOS-2) SAR images from Path32 Frame 3160 are used for this study. The data were acquired in SM1 mode and HH polarization from a descending orbit with an incidence angle of 38.2° off nadir. The delivered SAR images have a spatial resolution of 3 m and a width of 50 km. It covers part of China's Greater Bay area, including southern Dongguan, western Shenzhen, and northwest Hong Kong (see Fig. 1). A total of eight interferograms were formed using nine SAR images from 20170415 to 20180707 with the common reference image on 20171125 (row 1 in Fig. 2).

B. Spatially Segmented Scaling Approach for Topography-Dependent APS (SSSA-TD APS)

The height-dependent linear model and the power law model of stratified atmospheric delay can be written as

$$\Delta\phi_{\mathrm{s}}^{l} = k_h^{l} \cdot \Delta h + c \tag{1}$$

$$\Delta\phi_{\mathrm{s}}^{p} = k_h^{p} \cdot (h_r^{p} - h)^{\alpha} \tag{2}$$

where k_h^l and k_h^p are the coefficients for linear and power law relationship between phase and height, respectively. Δh is the

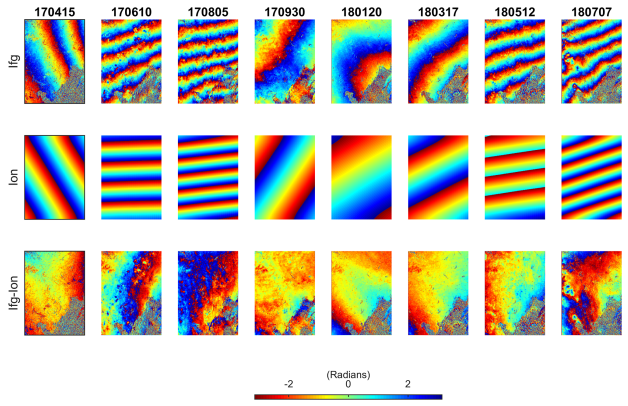

Fig. 2. Ionospheric delays for different interferograms formed with a common reference image on November 25, 2017. The first, second, and third rows are the original interferograms, the ionospheric phase estimated by the split spectrum method, and the ionospherically corrected interferograms, respectively.

height from digital elevation model (DEM) and c is the TD APS at DEM reference level. h is the power law model height. The power law reference height h_r^p and the power law coefficient α can be estimated from balloon sounding data [21].

A unified phase–height relationship can model some height-dependent atmospheric effects (Fig. 16 in the Appendix). However, the model may be biased if there is a nonlinear relationship between phase and height. The spatially segmented methods are, therefore, used in this case to accommodate spatial variations in topography dependence. However, patchy patterns and an overfitting of the topography-independent signals (turbulence) can be seen from the estimated atmospheric delays using spatial segmentation of regular grids and irregular quadtree blocks (see Fig. 17 in the Appendix).

To mitigate the influence of topography-independent signals during stratified signal estimation, a spatially segmented scaling approach (SSSA) through a combination of quadtree decomposition [30] and weighting factors [32] is used to model height-dependent atmospheric signals.

First, the DEM is downsampled to 900 m to reduce the number of bins from later quadtree decomposition.

Second, quadtree decomposition is implemented on the resampled DEM by thresholding the gradient, e.g., 100-m height change in this case. The bins whose height changes are less than the threshold remain unchanged and the bins whose height changes are greater than the threshold are divided into four quadrants. The process terminates when the height changes of all bins are less than the set threshold.

Third, a least squares inversion is performed between the deramped unwrapped phase and the persistent scatterer (PS) height to retrieve scaling factors in each quadtree bin. Note that although a downsampled DEM (900 m) is used for quadtree composition, the PS points are aligned with the height of original DEM (30 m) for TD APS estimation

$$\begin{bmatrix} k_i & c_i \end{bmatrix}^T = \begin{bmatrix} h_i & ones_i \end{bmatrix} \backslash uw_{i,\text{deramp}} \tag{3}$$

$$a(h)_i = k_i \cdot h_i + c_i. \tag{4}$$

Fourth, a weighting method combining distance, estimation uncertainty, and Gaussian filter [21], [32] is employed to smooth the scaling factors k_i and c_i. There are m patches for n PS points after quadtree decomposition. The estimated TD-APS and its residual phase with the deramped unwrapped phase are used to calculate the variance weighting factor in each quadtree patch i

$$w_{v,i} = \frac{\text{var}\left(a(h)_i\right)}{\text{var}\left(uw_{i,\text{deramp}} - a(h)_i\right)}, \quad i \in (1, m)\,. \tag{5}$$

The distance between each patch i and point j, along with a Gaussian filter, is used to calculate the distance weighting factor for that point

$$w_{d,i,j} = \frac{1}{2\pi\sigma^2}\, e^{-\frac{x_{i,j}^2 + y_{i,j}^2}{2\max\left(x_{i,j}^2 + y_{i,j}^2\right)}}, \quad j \in (1, n) \tag{6}$$

$$w_{a,i,j} = w_{v,i} \cdot w_{d,i,j} \tag{7}$$

where $x_{i,j}$ and $y_{i,j}$ are the coordinate differences between patch i and point j.

Different from previous weighting methods, this study not only combines the variance weighting factor and the distance weighting factor, but also normalizes them to generate a weighting matrix from each patch i to point j

$$k_j = \sum_{i=1}^{m} \frac{w_{a,i,j}}{\sum_{i=1}^{m} w_{a,i,j}} \cdot k_i \tag{8}$$

$$c_j = \sum_{i=1}^{m} \frac{w_{a(h),\,i,j}}{\sum_{i=1}^{m} w_{a(h),\,i,j}} \cdot c_i. \tag{9}$$

The weighting factors k_j and c_j of each point are the weighted sum of all quadtree patches.

$$a(h)_j = k_j \cdot h_j + c_j. \tag{10}$$

Fifth, the smoothed weighting factors are used to generate a scaled TD APS to mitigate patchy pattern and overfitting of the unwrapped phase.

C. Stepwise Estimation Approach for Topography Topography-Dependent APS (SWEA-TD APS)

As an alternative to the SSSA, an SWEA is proposed in this study to estimate TD atmospheric effects over a series of consecutive height intervals, rather than local windows, to avoid overfitting turbulence in coastal areas.

First, PS points are grouped by height intervals. In this case, with a height increment of 100 m, eight height intervals are formed from below 100 m to between 700 and 800 m.

Second, a least squares inversion is performed between the deramped unwrapped phase and the height to obtain scaling factors in each height group.

Third, if the estimates of scaling factors for lower height intervals are affected by significant turbulence signals, they are adjusted by extrapolation from other higher intervals.

Fourth, the weighted scaling factors are used to obtain scaled TD APS.

D. Tropospheric Delay Estimation From NWP Models

There are different refractivity models for calculating tropospheric delay using NWP models. The toolbox for reducing atmospheric InSAR noise (TRAIN) [20] used the refractivity model proposed by Smith and Weintraub [42]. Tropospheric delay is the integration of refractivity from ground to the upper

TABLE I
NWP MODELS AND PRODUCTS (AFTER [53])

MODEL/ PRODUCT	Temporal resolution (h)	Spatial resolution (°)	Pressure/Model levels	Hydrostatic delay	Wet delay	Data delay	Data coverage
ERA5	1	0.25×0.25	37	✓	✓	5 days	1979 –
ERA-Interim	6	0.75×0.75	37	✓	✓	Several months	January1979 – August 2019
MERRA2	6	0.625×0.5	42	✓	✓	1–2 months	1980 –
GACOS (HRES-ECMWF)	6	0.125×0.125	137	Stratified + Turbulent		5–10 h	1979 –

boundary of troposphere in terms of the following equations [42]:

$$N_{\text{total}} = N_{\text{hydrostatic}} + N_{\text{wet}} = k_1 \frac{P}{T} + k_2 \frac{e}{T} + k_3 \frac{e}{T^2} \tag{11}$$

$$\Delta L = \frac{-4\pi}{\lambda} \frac{10^{-6}}{\cos\theta} \int_{r_1}^{r_2} N_{\text{total}} ds = \frac{-4\pi}{\lambda} \frac{10^{-6}}{\cos\theta} \int_{r_1}^{r_2} \left(k_1 \frac{P}{T} + k_2 \frac{e}{T} + k_3 \frac{e}{T^2} \right) ds \tag{12}$$

where k_1, k_2, and k_3 are the constants for atmospheric refractive index, T is the temperature, e is the partial pressure of water vapor, and P is the dry pressure. The stratified delay is converted from zenith to line-of-sight (LOS) direction by radar incidence angle without considering bending effect. A factor of 2 is applied for two-way propagation.

Radar interferometry calculation tools (RINC) [43] used the refractivity model proposed by Bevis et al. [44], [45]; GACOS [46] used the refractivity model proposed by Berrada Baby et al. [47]. Different refractivity models are available for tropospheric delay calculation, though their differences would have limited significance [48]. This work uses TRAIN for NWP APS correction; the refractivity model parameters k_1, k_2, and k_3 are 0.776 (K/Pa), 0.716 (K/Pa), and 3.75e3 (K^2/Pa) respectively.

Two typical approaches are used in tropospheric delay estimation, including delay integration along the radar LOS path e.g., TRAIN, and an iterative tropospheric decomposition approach, e.g., GACOS [49].

Various NWP models are available for atmospheric corrections (see Table I). ERA-Interim (ERA-I) [50], ERA5 [51], MERRA2 [52], and NWP-generated APS correction product GACOS are supported by TRAIN. Some of the NWP models are used for stratified APS correction in this study.

ERA-I products resolve 0.75°×0.75° latitude/longitude grid and are available every 6 h at 00, 06, 12, and 18 UTC. ERA-I covers the period from January 1979 to August 2019 and is being phased out by ERA5. TRAIN supports the use of an application programming interface (API) to obtain ERA-I data. The acquired ERA-I data boundaries are 20°–26°N and 111°–117°E. They have 37 pressure levels between 1 and 1000 hPa at unequal intervals (about 12 layers below 125 hPa). The size of ERA-I data tiles retrieved from european centre for medium-range weather forecasts (ECMWF) API is 9×9×37 for longitude, latitude, and levels.

Due to the relocation of data center, the resources of ERA5 are migrated. ERA5 retrieval moves from ECMWF API to Copernicus climate data store (CDS) API. Therefore, ERA5 data from CDS are directed to TRAIN for ERA5 APS. The ERA5 dataset has a higher spatial and temporal resolution than ERA-I, with a spatial resolution of 0.25°×0.25° and a temporal resolution of 1 h. The 6°×6° ERA5 data tile retrieved from CDI is on a 25×25-point grid, and they have the same 37 levels as ERA-I.

MERRA2 dataset is retrieved from NASA GESDISC DATA ARCHIVE application with 0.5° latitude and 0.625° longitude resolution. MERRA2 data are available every 6 h at 00, 06, 12, and 18 UTC. The area setting for MERRA2 is 20°–26°N and 111.25–116.875°E on a 13×10-point grid. MERRA2 data provide 42 pressure levels (about 18 layers below 100 hPa).

The air temperature, geopotential, pressure level, and relative humidity in data tiles are used for NWP APS. Despite the resolution differences, the spatial patterns of ERA-I, ERA5, and MERRA2 parameters are visually similar. The geopotential is first converted to geopotential height and then to geometric height. Temperature, pressure, and humidity are interpolated in steps of 15 m from zero altitude to the upper troposphere at about 15-km altitude. These parameters are then used to calculate the hydrostatic and wet delays using numerical integration in the form of (12).

GACOS service provides delay files instead of NWP model parameters upon request with specified area, time of interest, and dates. The hydrostatic and wet components are combined as zenith total delay in GACOS products. GACOS products are distributed in a spatial resolution of 90 m.

E. Spatially Segmented Scaling Approach for Tropospheric Delays From NWP Models (SSSA-ERA5)

Scaling of NWP-simulated APS in height-dependent quadtree blocks helps reduce its difference with the unwrapped interferogram, but at the cost of overfitting the unwrapped interferogram. The SSSA that has been used for TD APS estimation is also used to scale ERA5 APS. SSSA-scaled ERA5 APS takes advantage of both topography gradient and ERA5 APS as follows.

First, the DEM is downsampled to a resolution comparable to the numerical weather model, e.g., about 900 m in this case, to match the 1-km resolution of ERA5.

Second, quadtree decomposition is implemented on the resampled DEM by setting a gradient threshold. The height change threshold in this case is 100 m.

Third, a least squares inversion is performed between the deramped unwrapped phase and the ERA5 APS to obtain the scaling factors in each quadtree bin.

Fourth, the scaling factors are weighted by distance, estimation uncertainty, and Gaussian filters and normalized to reduce patchy pattern and overfitting of the signal.

Fifth, the weighted scaling factors are used to obtain the scaled ERA5 APS.

F. Stepwise Estimation Approach for Tropospheric Delays From NWP Models (SWEA-ERA5)

Alternatively, an SWEA is proposed to estimate TD APS over multiple height intervals from the NWP models as follows:

First, PS points are grouped by height intervals. In this case, with a height increment of 100 m, eight height intervals are formed from below 100 m to between 700 and 800 m.

Second, a least squares inversion is performed between the deramped unwrapped phase and the ERA5 APS to obtain scaling factors in each height group.

Third, the weighted scaling factors are used to obtain the scaled ERA5 APS.

G. Tropospheric Correction Using MODIS Water Vapor Fields and HYSPLIT Air Mass Trajectories (MODIS+HYSPLIT)

GACOS estimates both stratified and turbulent signals using ECMWF's operational high-resolution atmospheric model (HRES). HRES occupies a horizontal resolution of 9 km and a vertical resolution 137 levels. The wavelength of topography-independent signals in coastal area is beyond the resolution of HRES. Alternatively, 1-km-resolution spectrometer water vapor fields by MODIS are employed for topography-independent signal study.

TRAIN suggested OSCAR JPL-MODIS service for MODIS spectrometer estimate. However, OSCAR MODIS service is no longer operational, and OSCAR is now an acronym assigned for ocean surface current analysis by JPL. Alternatively, MODIS water vapor product 05_L2 established by NASA is directed to TRAIN for water vapor delay [54], [55]. Combined with the trajectory information of HYSPLIT, the near-IR total column precipitable water vapor field with a spatial resolution of 1 km near the SAR acquisition time was displacement compensated and differenced to generate a water vapor difference map for interferogram.

The HYSPLIT trajectories are available upon request from the NOAA Air Resources Laboratory. The HYSPLIT trajectory model can use global or regional meteorological data, such as GDAS, GFS, REANALYSIS, etc. GDAS is an NCEP weather and climate model that interpolates data from various observing systems and instruments on a 3-D grid. We compute archive trajectories in a 6×6° matrix type using GDAS datasets at 1° (GDAS1) and 0.5° (GDAS0p5) resolution. Since the lower atmosphere carries more water vapor, the model parameters are set to a lower ground level, e.g., 50 m. The model was run for 3 or 4 h, spanning the period of two MODIS images. There are only individual differences in matrix elements between GDAS1 and GDAS0p5, and GDAS0p5 was chosen to ensure overall consistency between matrix elements.

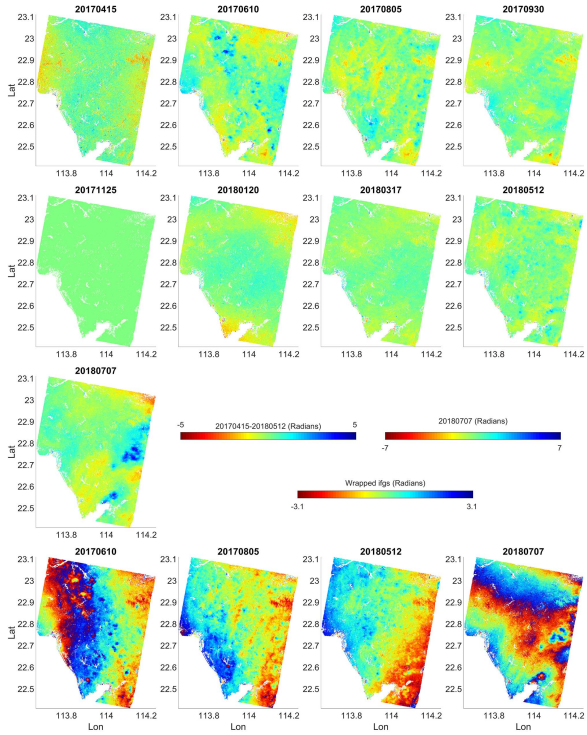

Fig. 3. Unwrapped interferogram after removing ionospheric effects by the split spectrum method and removing phase ramps by quadratic planes. The color range of the first to eighth interferograms is narrower than the color range of the ninth interferogram for better display. The wrapped phases of the second, third, eight, and ninth ionospherically corrected interferograms showing small-to-medium-scale heterogeneities are also given.

III. Results

Ionospheric corrected interferograms show a substantial decrease of fringe rate for all interferograms (see Fig. 2).

A series of interferograms with a common reference image on 20171125 are formed for each secondary image (see Fig. 3). The interferometric patterns vary greatly, indicating the presence of atmospheric effects. TD atmospheric effects, e.g., 20170930 (see Fig. 3) can be found in DaLing (DL) hill, GuanYin-YinPing (GY-YP) hills, YangTai-TangLang-YinHu (YT-TL-YH) hills, and LamTsuen-TaiLam (LT-TL) Hills (see Fig. 1). Small-scale (e.g., 2017061, 20170805, and 20180512) to medium-scale (e.g., 20180707) topography-independent heterogeneities can also be identified, which are discussed later in Section IV-C.

A. Stepwise Estimation Approach for Topography-Dependent APS (SWEA-TD APS)

The stepwise method models the TD APS by a multipiece linear function, and the results show a good approximation of the TD APS by the multipiece function with no gaps between adjacent intervals for interferogram 20171125–20170930 (see Fig. 4).

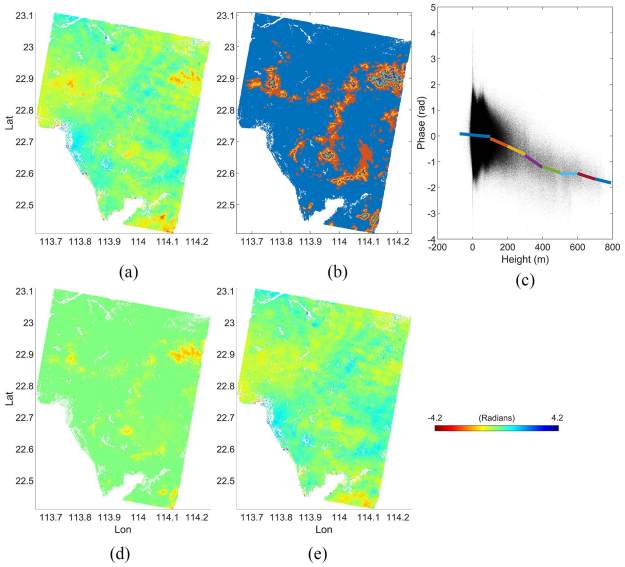

Fig. 4. TD APS estimated in stepwise height intervals for interferogram 20171125–20170930 (SWEA-TD). (a) Unwrapped phase after removing phase ramp. (b) SWEA height intervals. (c) Phase–height relationship and its multi-interval estimation. (d) SWEA-estimated height-dependent APS. (e) Residual phase.

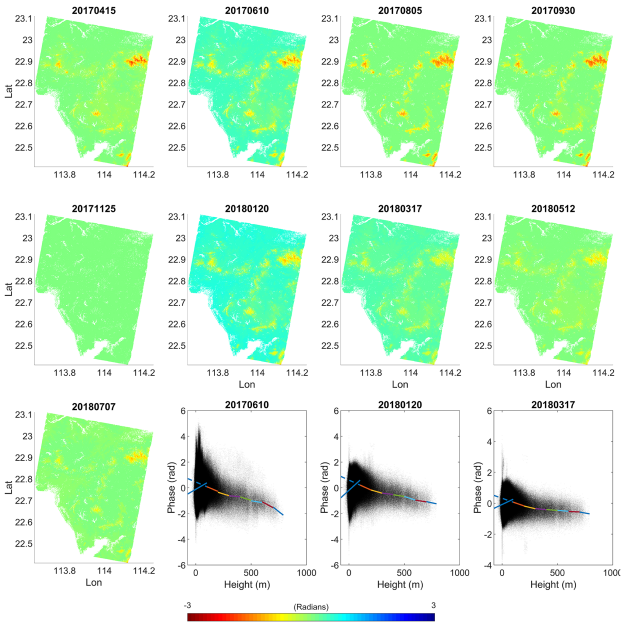

Fig. 5. TD APS estimated using a stepwise approach for a series of interferograms (SWEA-TD). The solid line in the last three panels is the topography dependence estimated by SWEA. The dashed line extrapolated topography dependence for the interval below 100 m.

The phase versus height relationship in the results for 20170610, 20180120, and 20180317 shows a sign change at 100-m height (see Fig. 5). Another study also observed a sign change of delay-to-height ratio but in a range of 1000–1500 m in Lake Mead [26], while, in this case, the sign change is around 100-m height. The rapid sign change and the limited sign length to the left of the sign change make it more likely to be the result of strong turbulence signals rather than real stratification changes.

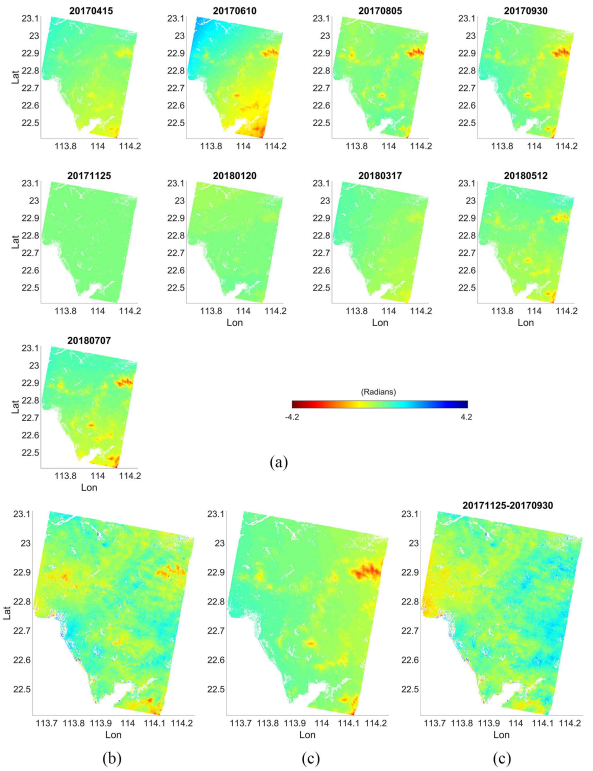

Fig. 6. (a) Tropospheric atmospheric delay estimated from the ERA5 model. (b)–(d) Deramped unwrapped phase, ERA5 APS, and residue for 20171125–20170930, respectively.

The humidity and temperature parameters of NWP models did not show similar stratification changes either. Alternatively, the topography dependence relationship in the interval of 100–200 m is assigned to the interval below 100 m to model TD APS (see Fig. 5).

B. Stepwise Estimation Approach for Stratified Tropospheric Delays From NWP Models (SWEA-ERA5)

NWP models can be used to simulate the atmospheric effects associated with each interferogram. ERA-I (see Fig. 18 in the Appendix), MERRA2 (see Fig. 19 in the Appendix), and ERA5 (see Fig. 6) show consistent APS pattern, with only minor differences in the amplitude of APS. However, with the exception of the scene formed in 20170930 [see Fig. 6(b)], most of the ERA5 simulated APS (see Fig. 6) fail to resemble the pattern of the interferograms (see Fig. 3). This indicates that NWP models mainly model the stratified atmospheric effects rather than topography-independent atmospheric effects due to limited spatial and temporal resolutions. The ERA5 APS is further scaled by the SWEA to better model tropospheric signals (see Fig. 7).

C. Comparison of SSSA-TD, SWEA-TD, SSSA-ERA5, and SWEA-ERA5.

For comparison, existing spatially segmented scaling methods SSSA-TD (see Fig. 8) and SSSA-ERA5 (see Fig. 9) are also implemented.

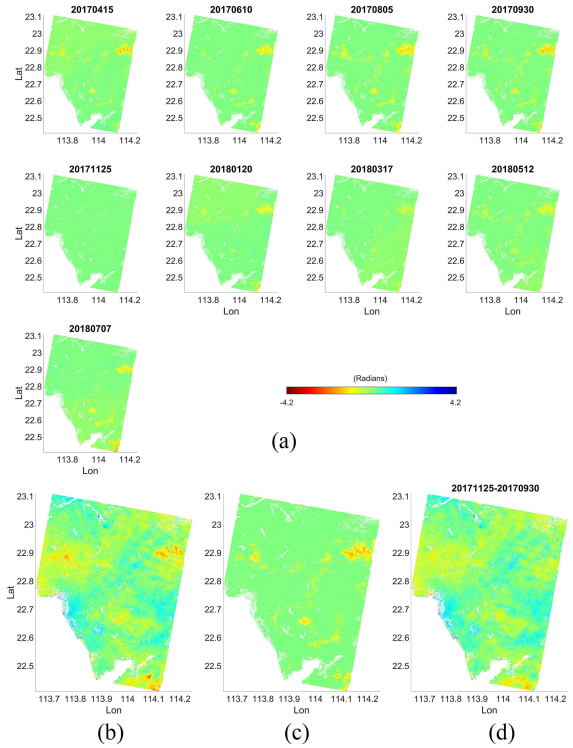

Fig. 7. (a) ERA5 APS scaled using a stepwise approach (SWEA-ERA5). (b)–(d) Deramped unwrapped phase, SWEA-ERA5 APS, and residue of interferogram 20171125–20170930, respectively.

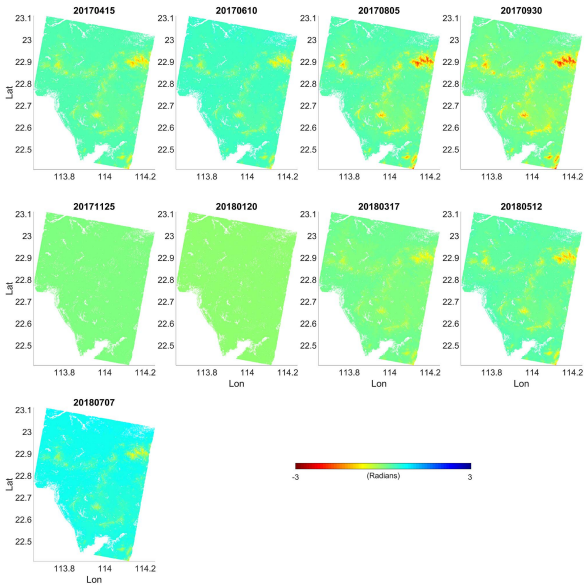

Fig. 8. TD APS for a series of interferograms estimated in quadtree blocks, and weighted by distance and variance (SSSA-TD).

The four tropospheric atmospheric effects' estimation or scaling approaches SSSA-TD, SWEA-TD, SSSA-ERA5, and SWEA-ERA5 are compared as follows.

1) SSSA-TD APS Versus SWEA-TD APS: The amplitude of SSSA-TD APS (see Fig. 8) is larger than SWEA-TD APS (see Fig. 5) in the higher elevation areas of interferogram 20180512, such as GY-YP hills. SSSA-TD APS is greater than or equal to

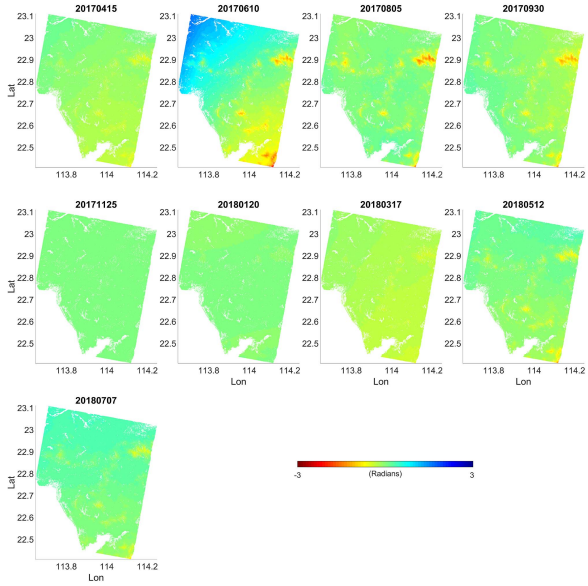

Fig. 9. ERA5 APS scaled in quadtree blocks and weighted by distance and variance (SSSA-ERA5).

SWEA-TD APS in interferograms 20170805 and 20170930 at higher altitudes (e.g., DL hills, GY-YP hills, YT-TL-HL, and LT-TL hills). SSSA-TD APS and SWEA-TD APS are comparable on interferogram 20180317.

When local strong topography-independent signals occur, as shown in the interferograms 20170415, 20170610, and 20180707, SSSA-TD APS exhibits smaller amplitudes than SWEA-TD APS in higher elevation regions (e.g., GY-YP hills). SSSA fails to model TD APS on 20180120 when it is affected by large-scale, smooth, topography-independent signals of similar amplitude.

In general, SWEA-TD can be less affected by topography-independent signals than SSSA-TD.

2) SSSA-TD APS Versus SSSA-ERA5 APS: The SSSA-TD APS (see Fig. 8) is similar to SSSA-ERA5 APS (see Fig. 9), but there are some differences in amplitude. In interferograms 20170415, 20180805, 20170930, 20180317, and 20180512, SSSA-TD APS outperforms SSSA-ERA5 APS in higher elevation areas (e.g., DL hills, GY-YP hills, YT-TL-HL, and LT-TL hills), possibly due to the lower resolution of ERA5 (1 km) compared to DEM (30 m).

SSSA-TD APS and SSSA-ERA5 APS are comparable on 20180707. They both fail on 20180120, and SSSA-ERA5 APS fails on 20180317 either.

The amplitude of SSSA-TD APS is smaller than the SSSA-ERA5 APS on the GY-YP and LT-TL hills in interferogram 20170610, possibly because the ERA5 corresponding to this interferogram also shows a long-wavelength mode of the NW-SE trending (see Fig. 6).

One advantage of SSSA-ERA5 is that the long-wavelength signals of ERA5 are preserved in SSSA-ERA5 (e.g., 20170610), although its trend is not necessarily consistent with the corresponding interferogram. But optimism is that if the long-wavelength stratified APS is well modeled by ERA5, it will also be kept in SSSA-ERA5.

TABLE II
STANDARD DEVIATION OF DERAMPED UNWRAPPED PHASE (UWDP) AND THE CORRECTED PHASE (C.P.) USING UNIFIED PHASE–HEIGHT RELATIONSHIP (UNI-TD), SSSA-TD, SWEA-TD, SWEA-TD∗, ERA5, SSSA-ERA5, AND SWEA-ERA5

	170415	170610	170805	170930	171125	180120	180317	180512	180707
UWDP	0.842	0.787	0.583	0.502	0.000	0.622	0.428	0.498	1.144
Uni-TD c. p.	0.833	0.786	0.571	0.486	0.000	0.621	0.428	0.492	1.143
SSSA-TD c. p.	0.833	0.788	0.573	0.488	0.000	0.621	0.432	0.493	1.145
SWEA-TD c. p.	0.833	0.773	0.568	0.484	0.000	0.594	0.419	0.492	1.142
SWEA-TD* c. p.		0.799				0.654	0.442		
ERA5 c. p.	0.934	1.102	0.581	0.547	0.000	0.619	0.475	0.549	1.182
SSSA-ERA5 c. p.	0.858	0.963	0.573	0.500	0.000	0.617	0.434	0.506	1.143
SWEA-ERA5 c. p.	0.831	0.781	0.568	0.485	0.000	0.614	0.426	0.493	1.137

SWEA-TD* denotes that the topography dependence relationship in the interval of 100-200 m is assigned to the interval below 100 m to model TD APS

3) SWEA-TD APS Versus SWEA-ERA5 APS: SWEA-TD APS (see Fig. 5) is comparable to SWEA-ERA5 APS (see Fig. 7), except for 20180707, which may be due to the presence of long-wavelength modes in its corresponding ERA5 APS.

4) SSSA-ERA5 APS Versus SWEA-ERA5 APS: For almost all pairs, SSSA-ERA5 APS (see Fig. 9) exhibits smaller amplitudes than SWEA-ERA5 APS (see Fig. 7) at high altitudes (e.g., GY-YP, DL, YT-TL-YH, and LT-TL hills). SWEA-ERA5 models height-dependent APS in higher altitudes better than SSSA-ERA5, but SWEA-ERA5 fails to preserve the long-wavelength pattern of ERA5 that can be preserved by SSSA-ERA5, such as 20170610.

The standard deviation of each interferogram was calculated using the tropospheric-corrected residual phase (see Table II). The standard deviations of the interferograms corrected by SSSA-TD are smaller than the standard deviations of the uncorrected interferograms except 20170610 and 20180317. The standard deviations of the interferograms corrected by SWEA-TD are all smaller than the standard deviation of the uncorrected interferograms, except that the topography dependence relationship in the interval of 100–200 m is assigned to the interval below 100 m for TD APS modeling (SWEA-TD∗ in Table II).

The standard deviations of the interferograms corrected by ERA5 directly are greater than the standard deviations of the uncorrected interferograms except for 20170805 and 20180120 (see Table II). The standard deviation of the SSSA-ERA5-corrected interferogram increases in half of the cases and decreases in the other half compared with the standard deviation of the uncorrected interferogram. The standard deviations of the interferograms corrected by SWEA-ERA5 are all smaller than the standard deviation of the uncorrected interferograms.

For interferogram 20171125–20170930, SSSA-TD APS and SWEA-TD APS help to scale TD-APS for hills such as DL, GY-YP, YT-TL-YH, and LT-TL without overfitting. TD APS scaled by SSSA or SWEA methods have smaller discontinuities than TD PAS obtained directly from quadtree blocks.

For this interferogram-stratified APS signals of the hills, such as DL, GY-YP, YT-TL-YH, and LT-TL hills can also be identified from ERA5 before applying SSSA or SWEA, but with obvious differences in amplitude (see Fig. 10). SWEA-ERA5 helps scale ERA5 APS. SSSA-ERA5 APS underestimates TD APS compared with SWEA-ERA5 APS. The TD-APS-corrected variograms show significant improvements in variance with respect to distance (see Fig. 10).

The land reclamation areas of Qianhai and Houhai in Shenzhen are subsiding [56]. Possible overfitting effects by the proposed methods on the deformation are also evaluated in Qianhai and Houhai areas in interferogram 20171125–20180512 (see Fig. 20 in the Appendix). The unscaled TD APS phase pattern estimated in quadtree blocks is similar to the interferometric pattern in the Qianhai region, but since the size of the quadtree block is larger than the deformation scale of this flat region, the effect of overfitting on the deformation is not obvious. The stratified atmospheric effects estimated by SSSA-TD, SWEA-TD, SSSA-ERA5, and SWEA-ERA5 do not exhibit overfitting to deformation.

D. Tropospheric Delays From MODIS Water Vapor Fields and HYSPLIT Air Mass Trajectories

This section shows the example of assessing tropospheric delay using MODIS (see Fig. 11) and HYSPLIT (see Fig. 12) when the pattern of interferogram [see Fig. 13(a)] differs from TD APS or NWP APS [see Fig. 13(b)]. The source-receptor air mass trajectory model HYSPLIT is used to track the movements of MODIS near-IR water vapor products MOD05_L2 and MYD05_L2 that are collected by Terra and Aqua platforms [54].

The observation time of ALOS-2 images used in this work is UTC 04:16, and the MODIS image time in this area that is close to ALOS-2 imaging time is usually around UTC 03:00 and UTC 06:00. Therefore, the MODIS images provide observations of water vapor field before and after ALOS-2 acquisition. A pair

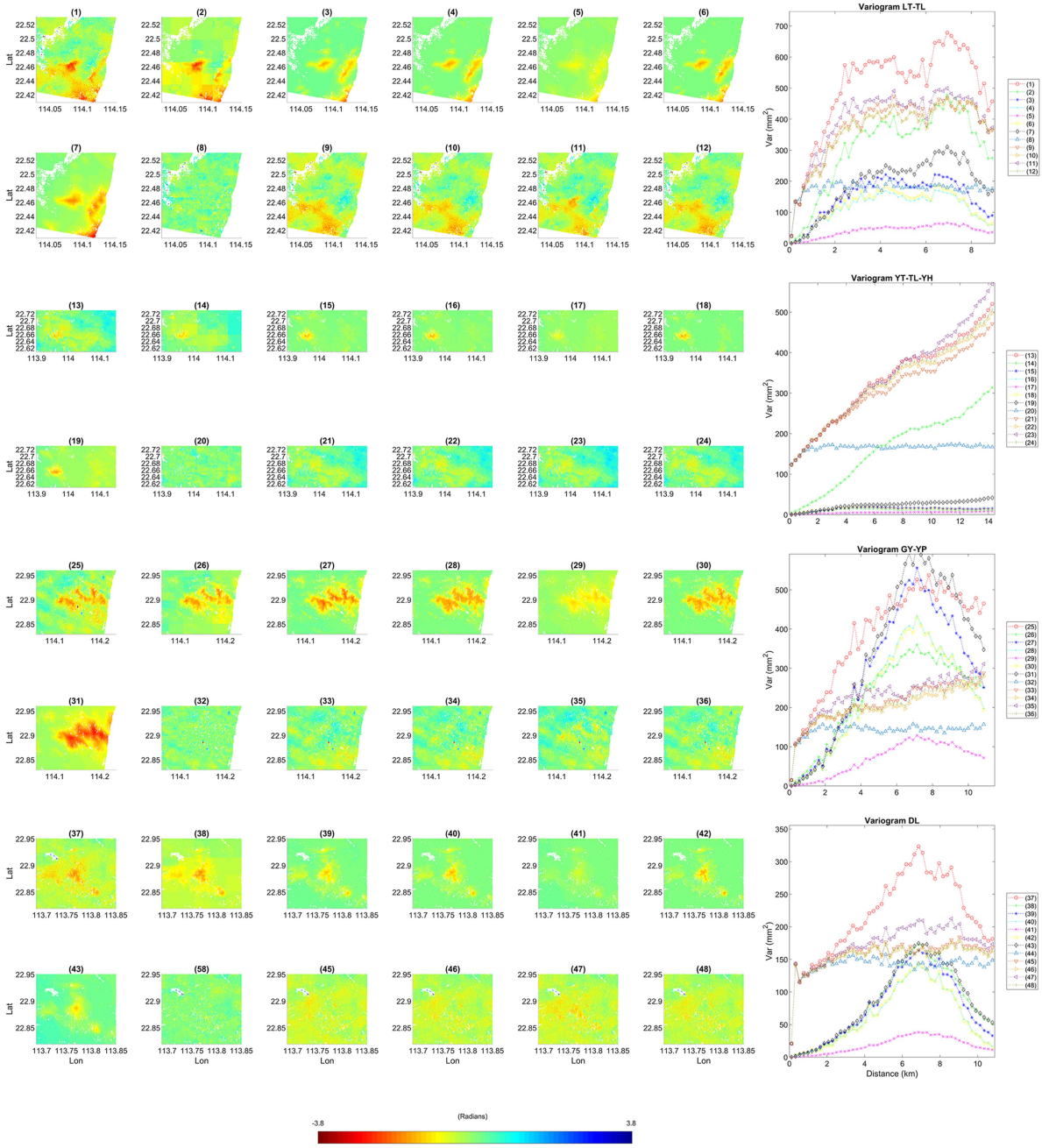

Fig. 10. Stratified APS estimation in hilly areas in interferogram 20171125–20170930. The TD APSs estimated from quadtree blocks without further scaling and the residuals are shown in column 2. SSSA-TD APS, SWEA-TD APS, SSSA-ERA5, and SWEA-ERA5 and the residuals are shown in columns 3–6, respectively. Panels (1)–(12) show the LamTsuen and TaiLam (LT-TL) areas. Panel (1) is the deramped unwrapped phase of LT-TL. Panel (7) is the ERA5 APS. Panels (2) and (8) are the TD APS estimated in quadtree blocks and its residuals from deramped unwrapped phase. Panels (3) and (9) are the SSSA scaled TD APS and its residuals. Panels (4) and (10) are the SWEA-estimated TD APS and its residuals. Panels (5) and (11) are the SSSA-scaled ERA5 APS and its residuals. Panels (6) and (12) are the SWEA-scaled ERA5 APS and its residuals. Panels (13)–(24) show the range of YangTai-TangLang-YinHu (YT-TL-YH) hills, in the same order as for Panels (1)–(12). Panels (25)–(36) show the range of GuanYin-YinPing (GY-YP) hills. Panels (37)–(48) show the range of DaLing (DL) hill. The variograms of the stratified APS estimated are given alongside the plots of LT-TL, YT-TL-YH, GY-YP, and DL hills, respectively. DL, GY-YP, YT-TL-YH, and LT-TL hills are outlined in Fig. 1.

of MODIS images before and after SAR imaging can be used to analyze the water vapor field of the ALOS-2 interferogram. The advantage of a pair of MODIS images over a single MODIS image is that the reliability of the MODIS water vapor field can be assessed (see Fig. 11).

MODIS images taken just a few hours apart are visually inspected. The correlation of water vapor fields at 03:50 and 05:20 UTC on September 30, 2017 and January 20, 2018 is stronger than that on other dates. Therefore, the differential water vapor fields are generated from the two pairs of MODIS images and further compared with their corresponding interferogram 20170930–20180120.

The MODIS-HYSPLIT approach to assess topography-independent signals is implemented as follows.

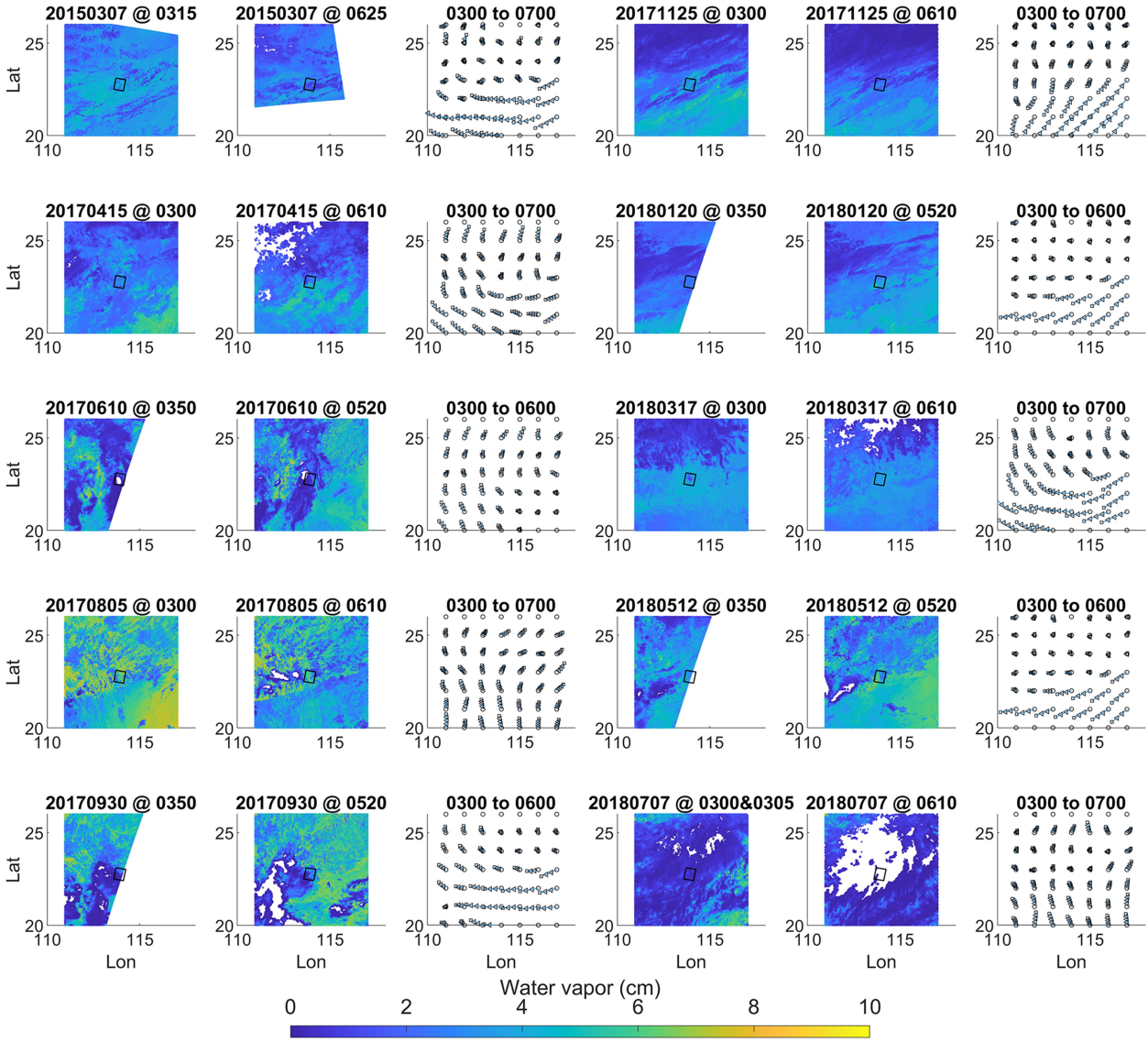

Fig. 11. MODIS water vapor near-IR and HYSPLIT trajectories covering this period. The temporal resolution of the trajectory matrix is 1 h, and the starting point, middle points, and end point of each trajectory are represented by circles, triangles, and squares, respectively.

First, the virtual water vapor field at the SAR acquisition time is derived from MODIS water vapor field considering the offsets of HYSPLIT between MODIS imaging time and SAR imaging time (see Fig. 12). For 20170930, the correlation coefficient between the 03:50 [see Fig. 12(a)] and 05:20 [see Fig. 12(d)] MODIS water vapor fields is 0.30 (169 pairs). After HYSPLIT correction [see Fig. 12(b) and (e)], the correlation coefficient between the 04:16 virtual water vapor field inferred from 03:50 [see Fig. 12(c)] and the 04:16 virtual water vapor field inferred from 05:20 [see Fig. 12(f)] is 0.48 (153 pairs). A rise of correlation between water vapor fields is seen for 20170930 after HYSPLIT correction.

Second, the virtual water vapor fields generated from the MODIS images taken before the SAR imaging time are differenced to generate a virtual water vapor difference map of the interferogram [see Fig. 13(f)]. The same operation is performed on MODIS images taken after the SAR imaging time to generate another virtual water vapor difference map of the interferogram [see Fig. 13(g)].

Third, although the two virtual water vapor difference maps have already been corrected by HYSPLIT, they are further weighted by the time baselines between MODIS and SAR acquisitions and superimposed to calculate a weighted water vapor difference map of the interferogram [see Fig. 13(h)].

The calibration coefficient of MODIS water vapor field is 6.2 [57]. The MODIS water vapor difference maps inferred from 03:50 and 05:20 and their weighted superimposed MODIS water vapor difference map show a larger phase gradient than the unwrapped interferogram. Additional scale factors can help reduce the discrepancy between the unwrapped phase and the MODIS water vapor difference map. The weighted water vapor difference map is scaled to the phase range of unwrapped interferogram 20170930–20180120. The difference in water vapor between the north and the south [see Fig. 13(h)]

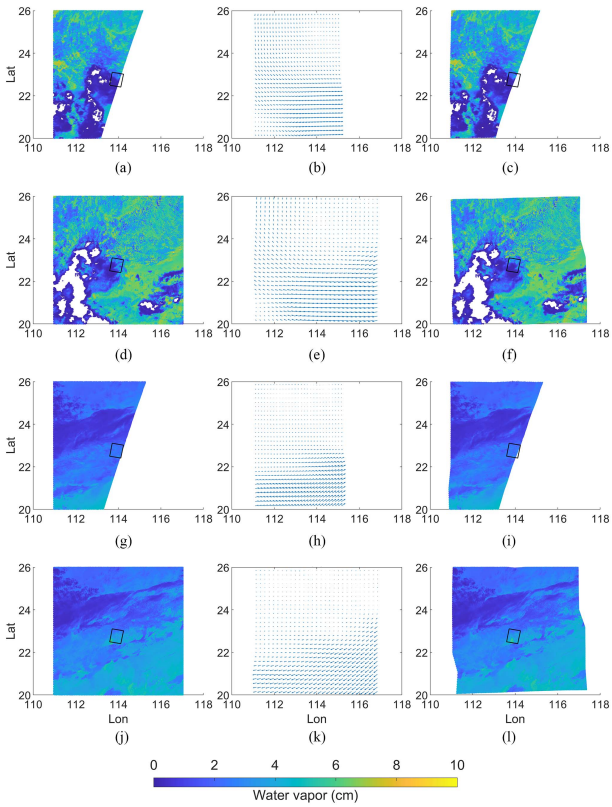

Fig. 12. MODIS water vapor fields of interferogram 20170930–20180120. The first column is the MODIS water vapor fields of 20170930 and 20180120. The second column is the air mass offsets of HYSPLIT air trajectory model from SAR acquisition time to MODIS image time. The third column is the virtual water vapor fields at the time of SAR acquisition. (a) MODIS water vapor field at 20170930 03:50. (b) HYSPLIT offsets from 20170930 04:16 to 03:50. (c) 20170930 04:16 virtual MODIS water vapor field inferred from 20170930 03:50. The same order as (a)–(c), (d)–(f) are MODIS+HYSPLIT at 20170930 05:20, (g)–(i) are MODIS+HYSPLIT at 20180120 03:50, and (j)–(l) are MODIS+HYSPLIT at 20180120 05:20.

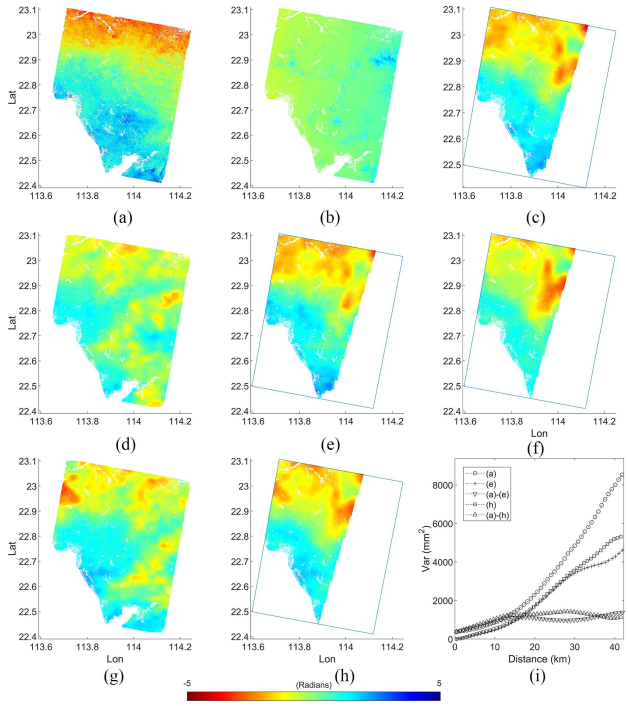

Fig. 13. (a) Unwrapped interferogram of 20170930–20180120. (b) ERA5 APS for interferogram 20170930–20180120. (c) 20170930–20180120 03:50 MODIS water vapor difference map. (d) 20170930–20180120 05:20 MODIS water vapor difference map. (e) Weighted superposition of water vapor difference maps (c) and (d). (f) Virtual water vapor difference map of 20170930–20180120 04:16 inferred from the MODIS water vapor difference map of 20170930–20180120 03:50 using the HYSPLIT air trajectory model. (g) Virtual water vapor difference map of 20170930–20180120 04:16 inferred from the MODIS water vapor difference map of 20170930–20180120 05:20 using the HYSPLIT air trajectory model. (h) Weighted superposition of water vapor difference maps (f) and (g). (i) Variograms of APS and unwrapped phase before and after APS correction using MODIS water vapor fields only or HYSPLIT-assisted MODIS near-IR water vapor fields.

can also be found in the unwrapped interferogram [see Fig. 13(a)].

IV. Discussion

Previous studies have shown that the atmospheric effects of InSAR are different in different climate zones. Water vapor is the major factor affecting InSAR atmospheric effects. Pressure and temperature are expected to cause smaller and evenly distributed atmospheric effects compared to tropospheric wet changes [11]. For example, in the polar regions, the atmospheric stratification is very stable and the cold air does not hold much water vapor, so the polar InSAR atmospheric effects are significantly different from the rest of the earth [58]. For most other places, water vapor changes less in dry areas, while water vapor content in wet areas varies greatly in space and time [11]. According to statistics from the Shenzhen Meteorological Observatory, the average annual precipitation in Shenzhen is 1932.9 mm, and the average annual precipitation days (the number of days with precipitation ≥ 0.1 mm) are 130.1 days. Therefore, the InSAR wet delay in this region can be significant.

Weather in coastal areas is another factor that affects InSAR atmospheric delays. Affected by atmospheric convection, rainfall and severe thunderstorms often occur in coastal areas. These turbulences also produce InSAR tropospheric delays. Hanssen [58], [59] reported that the tropospheric delay caused by thunderstorms in coastal areas of The Netherlands was several times greater than during calm weather without significant convection.

Water vapor irregularities and winds cause atmospheric delay heterogeneity. Previous studies found that water vapor irregularities are "frozen" into the atmosphere and carried by prevailing winds [11], [60], producing both spatial and temporal variability.

The study area is in a subtropical coastal environment, and tropospheric delays are expected to occur due to multiple factors mentioned earlier. The tropospheric delay in this region and its influencing factors are discussed further below, e.g., stratified delay and height (water vapor), topography-independent tropospheric delays (turbulence), and possible cloud and wind pattern (water vapor irregularities).

A. Stratified Delays and Height

The ERA5 wet delay variation is an order of magnitude higher than ERA5 dry delay variation (see Fig. 21 in the Appendix). The ERA5 wet delay versus height relationship has a similar trend to the InSAR-derived phase versus height relationship (see

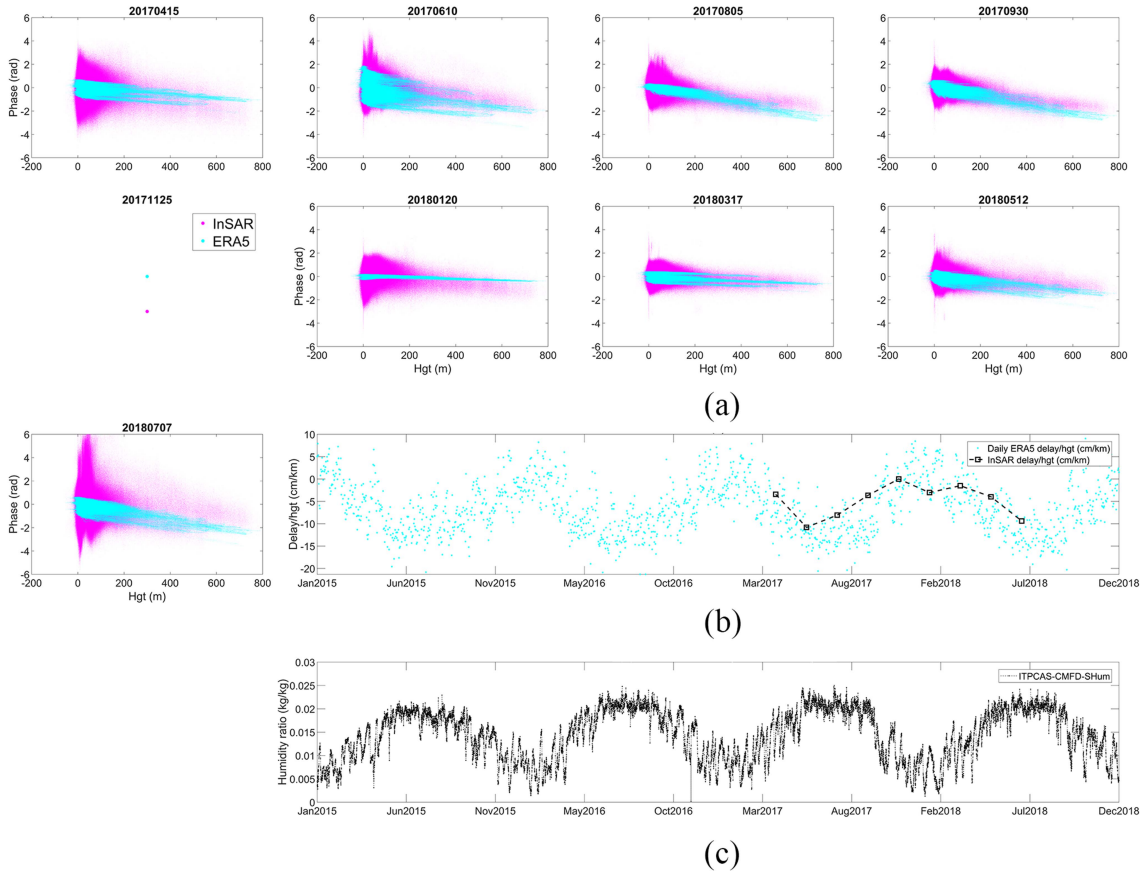

Fig. 14. (a) InSAR unwrapped phases and their corresponding ERA5 APS versus height in a series of interferograms. The ERA5 values are not scaled but double differenced to the same reference level of InSAR. (b) Daily ERA5 delay-to-height ratios and InSAR delay-to-height ratios. (c) Near-surface air-specific humidity closest to the center of the study area published by ITPCAS-CMFD dataset with a temporal resolution of 3 h [61].

Fig. 21), as the wet delay variation contributes most to the total delay variation.

We calculate the delay-to-height ratio for each interferogram using InSAR phase and height changes (see Fig. 14). The InSAR delay-to-height ratio of reference image date 20171125 is assigned zero as a reference. The delay-to-height ratios can be estimated from height bins at different height intervals. However, the interferometric phase of the lower height bins can be easily affected by turbulence. To avoid the influence of topography-independent signals, the InSAR delay-to-height ratio is averaged only from the upper two height intervals in the range of 600–700 m and 700–800 m in the stepwise estimation approach (SWEA-TD APS).

We calculate the daily ERA5 delay-to-height ratio from 2015 to 2018 using the nearest ERA5 files before (UTC 04:00) and after (UTC 05:00) SAR acquisition times (UTC 04:16). Since the InSAR phase is double differenced in space and time, the ERA5 daily delay is also double differenced to be comparable with InSAR. Temporally, the ERA5 delay on InSAR reference date of 20171125 is set as the reference in ERA5 delay series. Spatially, the mean value of each delay is set as its reference.

The InSAR delay-to-height ratios also follow the trend of ERA5 delay-to-height ratios [see Fig. 14(b)]. Generally, the tropospheric delay-to-height ratio curvature reaches a trough in summer, which means that the phase delay of the same thickness of the atmosphere is greater in summer than in winter. It can be seen from (11) that the water vapor partial pressure is positively correlated with the phase delay. The near-surface air-specific humidity of China meteorological forcing dataset (CMFD) for the same period shows that the humidity increases in the study area in summer [see Fig. 14(c)] [61], [62].

InSAR-derived stratified tropospheric delay-to-height ratios range up to 10.8 cm/km. Another study showed that stratified tropospheric delay-to-height ratio ranges were 5, 6, and 12 cm/km in the Lake Mead area, Haiyuan, and Afar regions, respectively [26]. There are regional differences in the delay-to-height ratio.

B. *Topography-Independent Tropospheric Delays*

ERA5 can be used to model long-wavelength and TD APS signals, while topography-independent signals can also be significant in the subtropical coastal environment. This can also be seen from the phase–height distribution of each interferogram. The interferograms exhibit a wider phase range than that of ERA5, especially for lower altitude regions (see Fig. 14).

In this case, according to the HYSPLIT model, the air mass can travel up to tens of kilometers between the SAR and MODIS acquisition times. The rise in correlation of MODIS water vapor

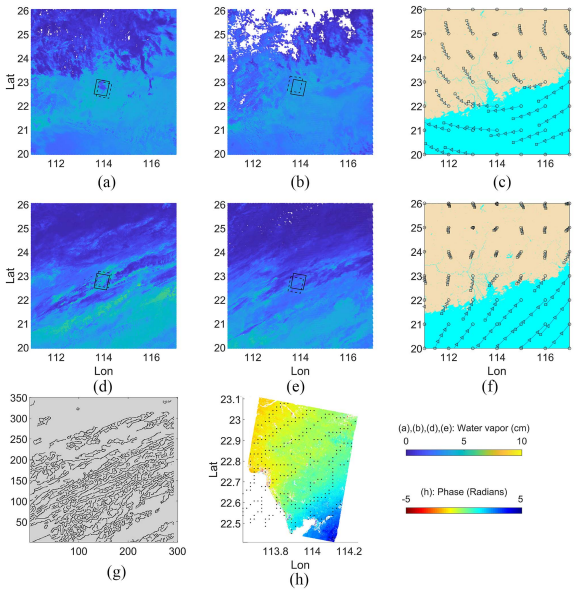

Fig. 15. Wind pattern in interferogram 20180317–20171125. (a) 20180317 03:00 UTC MODIS water vapor field. The solid rectangle is the InSAR frame and the dashed rectangle is the InSAR frame considering the motion of the nearest HYSPLIT element. (b) 20180317 06:10 UTC MODIS water vapor field. (c) 20180317 03:00 to 07:00 UTC HYSPLIT trajectory. (d) 20171125 03:00 UTC MODIS water vapor field. (e) 20171125 06:10 UTC MODIS water vapor field. (f) 20171125 03:00 to 07:00 UTC HYSPLIT trajectory. (g) Edges extracted from 20171125 03:00 MODIS water vapor field. (h) Extracted edges superimposed on the unwrapped phase.

fields after HYSPLIT correction indicates the necessity of considering air mass movement when using MODIS to analyze tropospheric delay. MODIS- or MODIS+HYSPLIT-corrected variogram shows a substantial improvement in distance-dependent variance beyond 20 km [see Fig. 13(i)]. The uncertainty in the HYSPLIT+ MODIS water vapor field can be attributed to turbulence (i.e., atmospheric convection) that are more complicated than horizontal movement (i.e., atmospheric advection), the accuracy of water vapor field itself, and the spatiotemporal resolution of the HYSPLIT model. Nonetheless, it still provides a finer resolution of the water vapor field than global numerical weather models and can sometimes provide a better approximation of the APS.

C. Possible Cloud and Wind Pattern

Some kilometer-scale small-scale heterogeneities can be identified, e.g., 20170610 and 20170805 (see Fig. 3). These heterogeneities do not stay in the same place and are not likely to be consistent displacements or TD APS. The PS points shown were selected according to time-series coherence and the heterogeneities are spatially correlated, so they are unlikely to be decorrelation noise either. Furthermore, these heterogeneities can also be found in the wrapped interferogram (see Fig. 3), so they are not phase unwrapping errors. Small-scale heterogeneities appear on 20170610 and 20170805, and the medium-scale phase delay appears on 20180707, when Shenzhen was in a hot and humid summer. We, therefore, suspect that the kilometer-scale turbulences may be the phase delay of radar waves passing through isolated clouds.

The phase pattern of interferogram 20180317–20171125 looks like a phase ramp from orbit error. Given that the precision of ALOS-2 precise orbit product after 2015 is better than 5 cm (RMS) [63], the phase ramp may not be caused by orbit errors. The edge extracted from MODIS near-IR water vapor field on November 25, 2011 is spatially correlated with the phase pattern observed in interferogram 20180317–20171125, and the edge direction is similar to the direction of the phase constant of the interferogram (see Fig. 15). The direction of phase constant agrees well with the northeast trade winds from the subtropical high to the equator. This is also confirmed by the contemporary HYSPLIT model. Therefore, the phase ramp can be lateral heterogeneities associated with NE Trade winds. Unfortunately, only one pair of phase ramp is found, as it also requires that the phase pattern of the other image in this interferometric pair does not obscure the ramp. We suspect that this is a wind pattern, but there is no guarantee, and we will leave this to the future to see if we can find more phase ramps associated with water vapor field and wind direction.

In addition to air mass trajectories, NWP models also provide wind speed information. Wind direction fields at multiple model heights are synthesized using the eastward and northward wind speed fields from MERRA2 (see Fig. 22 in the Appendix).

V. Conclusion

The atmospheric effects of ALOS-2 interferograms in Shenzhen are investigated in the study. For stratified tropospheric delay, a stepwise approach to estimate stratified atmospheric effects based on their height dependence or to scale NWP models is proposed and compared with the existing spatial segmentation approach. Both the stepwise and spatial segmentation approaches can reduce the TD APS using DEM or NWP.

For the dataset used here, the stepwise method gives better correction results than the spatial segmentation method, with smaller global standard deviation and more robust estimates in the presence of turbulence. SWEA methods are recommended when the topography-independent APS is significant. For the stepwise approach, the TD APS from DEM is slightly better than or equivalent to the APS of the NWP models in terms of global standard deviation.

For the spatial segmentation method, the TD APS derived from the DEM is better than the APS derived from NWP model, with smaller global standard deviation and no significant local underestimation. DEM is recommended for SSSA when the rate of height change exceeds the resolution of NWP. If long-wavelength modes are present in the APS and can be modeled well by NWP, it is recommended to use NWP for SSSA instead of DEM. SSSA-NWP is also better suited than SWEA-NWP to preserve the long-wavelength modes in NWP.

For the topography-independent APS, the MODIS water vapor field can be closer to the APS than the NWP model. MODIS water vapor products can be combined with HYSPLIT air mass trajectory models to mitigate the water vapor inconsistency caused by the time difference between SAR and spectrometer observations. Better correlation of MODIS images separated by several hours can be achieved after applying HYSPLIT correction. Both the weighted differential MODIS water vapor field and the HYSPLIT-assisted weighted differential MODIS water vapor field show similar trends to the interferogram.

Furthermore, this article suspects that kilometer-scale heterogeneities may be cloud patterns, and image-scale phase ramp may be wind patterns.

APPENDIX

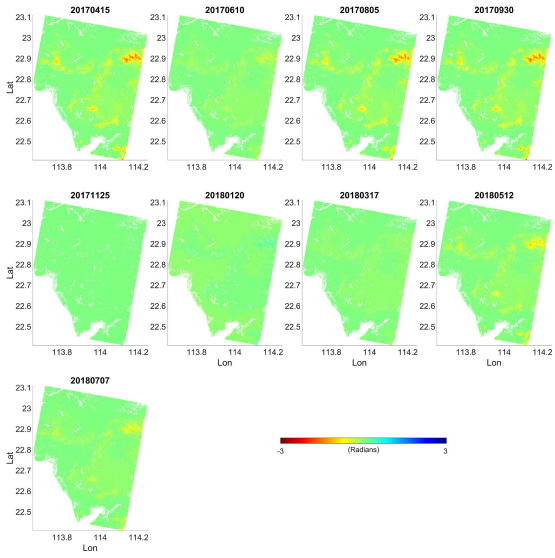

Fig. 16. TD APS estimated from a single linear phase–height relationship for each interferogram.

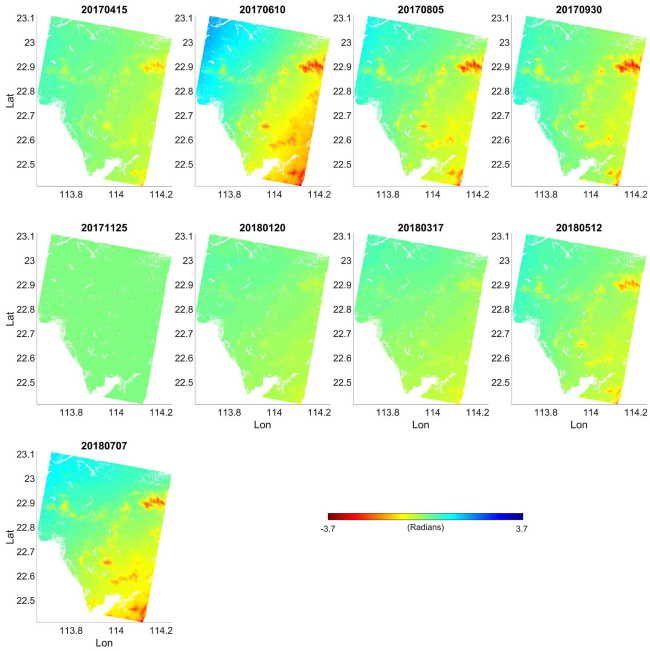

Fig. 18. ERA-Interim APS.

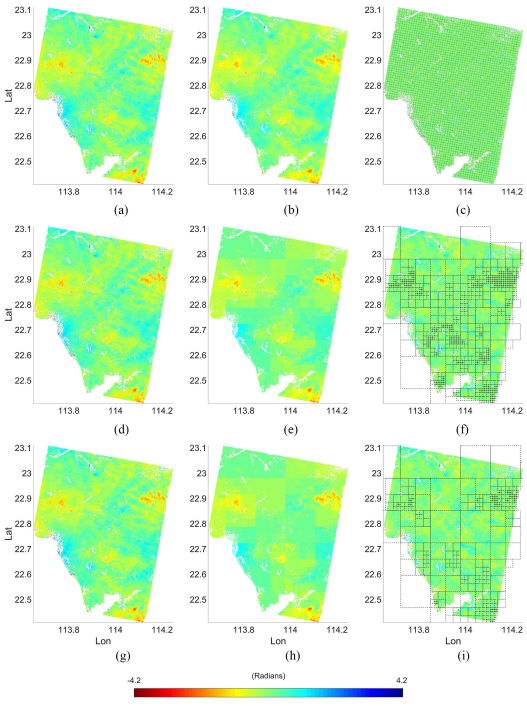

Fig. 17. Estimation of TD APS in interferogram 20171125–20170930 in segmented windows. The first row corresponds to the case where the stratified APS is estimated using a regular grid with a step size of 1 km. The second row corresponds to the case of quadtree decomposition with 100 m as its height variation threshold. The third row corresponds to the case that quadtree decomposition is completed with 200 m as its height change threshold. The three columns from left to right are the unwrapped phase, the modeled APSs, and their residuals, respectively.

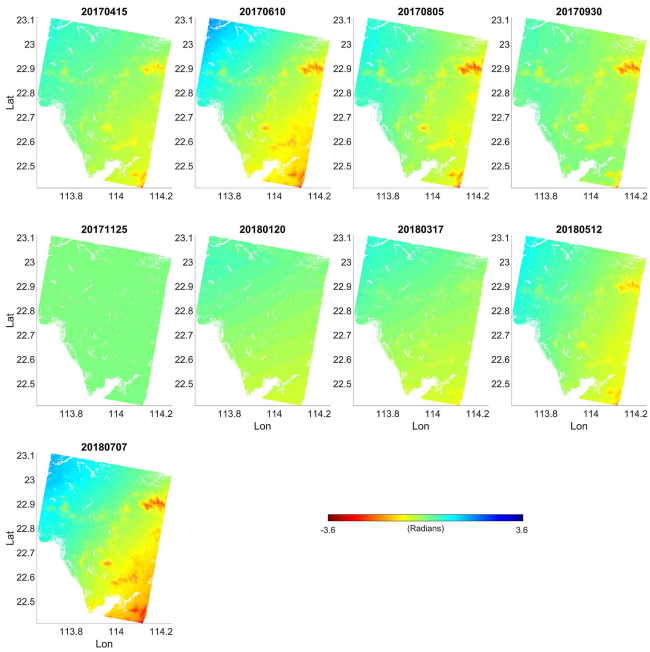

Fig. 19. MERRA2 APS.

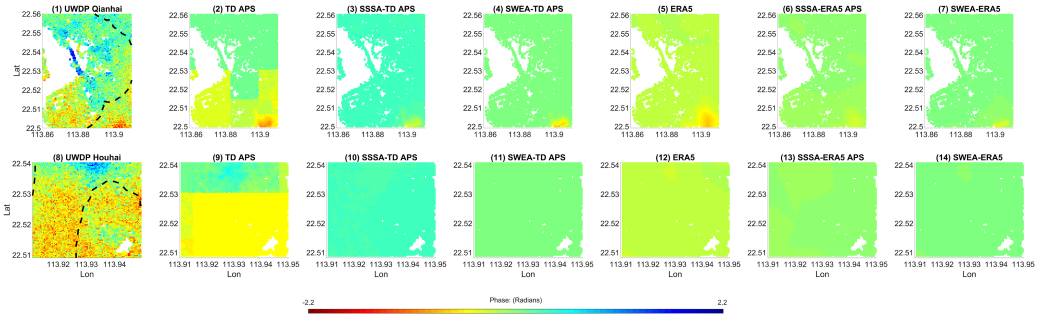

Fig. 20. Stratified APS estimation in land reclamation areas in interferogram 20171125–20180512. The dashed lines in panels (1) and (8) are the coastline in 1979. Panels (1)–(7) show the Qianhai area. Panels (8)–(14) show the Houhai area.

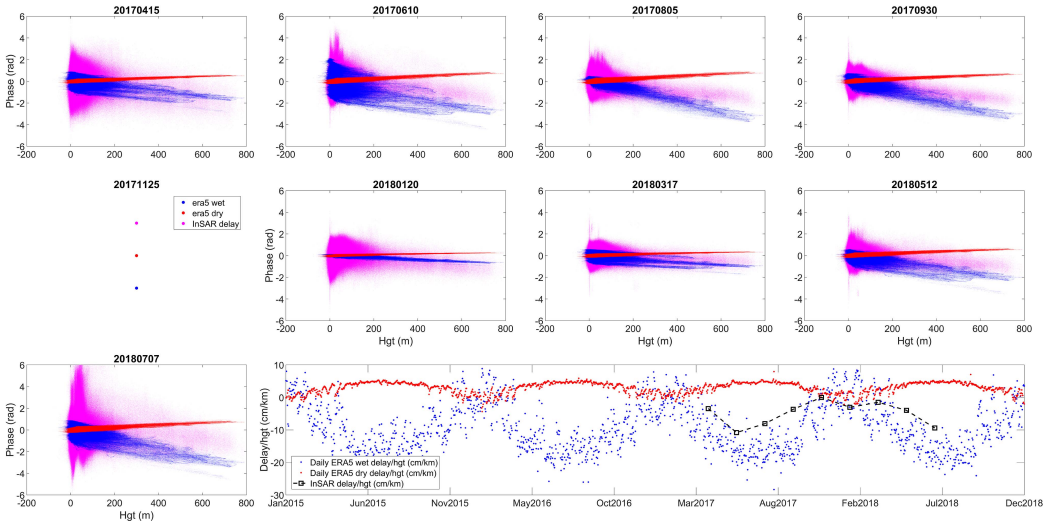

Fig. 21. Distribution of InSAR unwrapped phase, ERA5 dry delay, and wet delays with height, and their phase-to-height ratios.

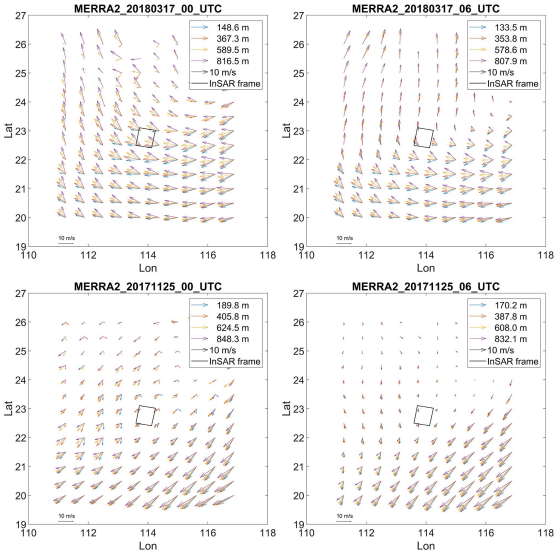

Fig. 22. Four different levels of wind speed and direction fields in MERRA2. Each level is marked with its average height.

ACKNOWLEDGMENT

The authors would like to thank the Japan Aerospace Exploration Agency for providing SAR data through the 6th ALOS-2 Research Announcement for ALOS-2 (RA6 PI No. 3164) and the 3rd Research Announcement on the Earth Observation (EORA3 PI No. ER3A2N131).

REFERENCES

[1] U. Wegmuller, C. Werner, T. Strozzi, and A. Wiesmann, "Ionospheric electron concentration effects on SAR and INSAR," in *Proc. IEEE Int. Symp. Geosci. Remote Sens.*, 2006, pp. 3731–3734.

[2] W. E. Gordon, "Incoherent scattering of radio waves by free electrons with applications to space exploration by radar," *Proc. IRE*, vol. 46, no. 11, pp. 1824–1829, 1958.

[3] H. G. Booker, "Fitting of multi-region ionospheric profiles of electron density by a single analytic function of height," *J. Atmos. Terr. Phys.*, vol. 39, no. 5, pp. 619–623, 1977.

[4] M. Hernández-Pajares et al., "The ionosphere: Effects, GPS modeling and the benefits for space geodetic techniques," *J. Geodesy*, vol. 85, pp. 887–907, 2011.

[5] C. Liang, P. Agram, M. Simons, and E. J. Fielding, "Ionospheric correction of InSAR time series analysis of C-band sentinel-1 TOPS data," *IEEE Trans. Geosci. Remote Sens.*, vol. 57, no. 9, pp. 6755–6773, Sep. 2019.

[6] P. A. Rosen, S. Hensley, and C. Chen, "Measurement and mitigation of the ionosphere in L-band interferometric SAR data," in *Proc. IEEE radar Conf.*, 2010, pp. 1459–1463.

[7] F. Meyer, R. Bamler, N. Jakowski, and T. Fritz, "The potential of low-frequency SAR systems for mapping ionospheric TEC distributions," *IEEE Geosci. Remote Sens. Lett.*, vol. 3, no. 4, pp. 560–564, Oct. 2006.

[8] A. L. Gray, K. E. Mattar, and G. Sofko, "Influence of ionospheric electron density fluctuations on satellite radar interferometry," *Geophys. Res. Lett.*, vol. 27, no. 10, pp. 1451–1454, 2000.

[9] E. J. Rignot, "Effect of Faraday rotation on L-band interferometric and polarimetric synthetic-aperture radar data," *IEEE Trans. Geosci. Remote Sens.*, vol. 38, no. 1, pp. 383–390, Jan. 2000.

[10] G. Gomba, A. Parizzi, F. De Zan, M. Eineder, and R. Bamler, "Toward operational compensation of ionospheric effects in SAR interferograms: The split-spectrum method," *IEEE Trans. Geosci. Remote Sens.*, vol. 54, no. 3, pp. 1446–1461, Mar. 2016.

[11] H. A. Zebker, P. A. Rosen, and S. Hensley, "Atmospheric effects in interferometric synthetic aperture radar surface deformation and topographic maps," *J. Geophys. Res. Solid Earth*, vol. 102, no. B4, pp. 7547–7563, 1997, doi: 10.1029/96jb03804.

[12] Z. Li et al., "Time-series InSAR ground deformation monitoring: Atmospheric delay modeling and estimating," *Earth Sci. Rev.*, vol. 192, pp. 258–284, May 2019, doi: 10.1016/j.earscirev.2019.03.008.

[13] R. Xiao, C. Yu, Z. Li, M. Jiang, and X. He, "InSAR stacking with atmospheric correction for rapid geohazard detection: Applications to ground subsidence and landslides in China," *Int. J. Appl. Earth Observ. Geoinf.*, vol. 115, 2022, Art. no. 103082.

[14] Y. Cao, Z. Li, and F. Amelung, "Mapping ground displacement by a multiple phase difference-based InSAR approach: With stochastic model estimation and turbulent troposphere mitigation," *J. Geodesy*, vol. 93, pp. 1313–1333, 2019.

[15] Y. Cao, Z. Li, J. Wei, J. Hu, M. Duan, and G. Feng, "Stochastic modeling for time series InSAR: With emphasis on atmospheric effects," *J. Geodesy.*, vol. 92, pp. 185–204, Aug. 2017, doi: 10.1007/s00190-017-1055-5.

[16] M. Duan et al., "Adaptively selecting interferograms for SBAS-InSAR based on graph theory and turbulence atmosphere," *IEEE Access*, vol. 8, pp. 112898–112909, 2020.

[17] Y. Chen, L. Bruzzone, L. Jiang, and Q. Sun, "ARU-net: Reduction of atmospheric phase screen in SAR interferometry using attention-based deep residual U-Net," *IEEE Trans. Geosci. Remote Sens.*, vol. 59, no. 7, pp. 5780–5793, Jul. 2021.

[18] A. Hooper, P. Segall, and H. A. Zebker, "Persistent scatterer interferometric synthetic aperture radar for crustal deformation analysis," *J. Geophys. Res. Solid Earth*, vol. 112, no. B7, pp. 1–21, 2007.

[19] Z. Li, M. Duan, Y. Cao, M. Mu, X. He, and J. Wei, "Mitigation of time-series InSAR turbulent atmospheric phase noise: A review," *Geodesy Geodyn.*, vol. 13, no. 2, pp. 93–103, 2022.

[20] D. P. S. Bekaert, R. J. Walters, T. J. Wright, A. J. Hooper, and D. J. Parker, "Statistical comparison of InSAR tropospheric correction techniques," *Remote Sens. Environ.*, vol. 170, pp. 40–47, 2015.

[21] D. P. S. Bekaert, A. Hooper, and T. J. Wright, "A spatially variable power law tropospheric correction technique for InSAR data," *J. Geophys. Res. Solid Earth*, vol. 120, no. 2, pp. 1345–1356, 2015, doi: 10.1002/2014JB011558.

[22] R. Jolivet et al., "Improving InSAR geodesy using global atmospheric models," *J. Geophys. Res. Solid Earth*, vol. 119, no. 3, pp. 2324–2341, 2014.

[23] R. Jolivet, R. Grandin, C. Lasserre, M. P. Doin, and G. Peltzer, "Systematic InSAR tropospheric phase delay corrections from global meteorological reanalysis data," *Geophys. Res. Lett.*, vol. 38, no. 17, 2011, Art. no. L17311, doi: 10.1029/2011gl048757.

[24] J. Jung, D.-j. Kim, and S.-E. Park, "Correction of atmospheric phase screen in time series InSAR using WRF model for monitoring volcanic activities," *IEEE Trans. Geosci. Remote Sens.*, vol. 52, no. 5, pp. 2678–2689, May 2014.

[25] Y. Cao, S. Jónsson, and Z. Li, "Advanced InSAR tropospheric corrections from global atmospheric models that incorporate spatial stochastic properties of the troposphere," *J. Geophys. Res. Solid Earth*, vol. 126, no. 5, 2021, Art. no. e2020JB020952.

[26] M.-P. Doin, C. Lasserre, G. Peltzer, O. Cavalié, and C. Doubre, "Corrections of stratified tropospheric delays in SAR interferometry: Validation with global atmospheric models," *J. Appl. Geophys.*, vol. 69, no. 1, pp. 35–50, 2009.

[27] Z. Li, E. J. Fielding, P. Cross, and J.-P. Muller, "Interferometric synthetic aperture radar atmospheric correction: Medium resolution imaging spectrometer and advanced synthetic aperture radar integration," *Geophys. Res. Lett.*, vol. 33, no. 6, pp. 1–4, 2006, doi: 10.1029/2005GL025299.

[28] C. Yu, N. T. Penna, and Z. Li, "Generation of real-time mode high-resolution water vapor fields from GPS observations," *J. Geophys. Res. Atmos.*, vol. 122, no. 3, pp. 2008–2025, 2017, doi: 10.1002/2016JD025753.

[29] C. Yu, Z. Li, N. T. Penna, and P. Crippa, "Generic atmospheric correction model for interferometric synthetic aperture radar observations," *J. Geophys. Res. Solid Earth*, vol. 123, no. 10, pp. 9202–9222, 2018.

[30] H. Liang, L. Zhang, X. Ding, Z. Lu, and X. Li, "Toward mitigating stratified tropospheric delays in multitemporal InSAR: A quadtree aided joint model," *IEEE Trans. Geosci. Remote Sens.*, vol. 57, no. 1, pp. 291–303, Jan. 2019.

[31] H. Liang, L. Zhang, Z. Lu, and X. Li, "Correction of spatially varying stratified atmospheric delays in multitemporal InSAR," *Remote Sens. Environ.*, vol. 285, 2023, Art. no. 113382.

[32] L. Shen, A. Hooper, and J. Elliott, "A spatially varying scaling method for InSAR tropospheric corrections using a high-resolution weather model," *J. Geophys. Res. Solid Earth*, vol. 124, no. 4, pp. 4051–4068, 2019.

[33] Z. Li, J.-P. Muller, P. Cross, and E. J. Fielding, "Interferometric synthetic aperture radar (InSAR) atmospheric correction: GPS, moderate resolution imaging spectroradiometer (MODIS), and InSAR integration," *J. Geophys. Res. Solid Earth*, vol. 110, no. B3, pp. 1–10, 2005, doi: 10.1029/2004JB003446.

[34] F. Onn and H. Zebker, "Correction for interferometric synthetic aperture radar atmospheric phase artifacts using time series of zenith wet delay observations from a GPS network," *J. Geophys. Res. Solid Earth*, vol. 111, no. B9, pp. 1–16, 2006.

[35] G. I. Taylor, "The spectrum of turbulence," *Proc. Roy. Soc. London, Ser. A*, vol. 164, no. 919, pp. 476–490, 1938.

[36] L. Chang and X. He, "InSAR atmospheric distortions mitigation: GPS observations and NCEP FNL data," *J. Atmos. Sol. Terr. Phys.*, vol. 73, no. 4, pp. 464–471, Mar. 2011, doi: 10.1016/j.jastp.2010.11.003.

[37] R. Draxler and G. Rolph, "HYSPLIT (HYbrid Single-Particle Lagrangian Integrated Trajectory) model access via NOAA ARL READY website," NOAA Air Resources Laboratory, Silver Spring, MD, USA, vol. 25, 2010. [Online]. Available: http://ready.arl.noaa.gov/HYSPLIT.php

[38] A. Stein, R. R. Draxler, G. D. Rolph, B. J. Stunder, M. Cohen, and F. Ngan, "NOAA's HYSPLIT atmospheric transport and dispersion modeling system," *Bull. Amer. Meteorol. Soc.*, vol. 96, no. 12, pp. 2059–2077, 2015.

[39] L. Li, Y. Liu, and Y. Wang, "Monitoring an air pollution episode in Shenzhen by combining MODIS satellite images and the HYSPLIT model," *IOP Conf. Ser.: Earth Environ. Sci.*, vol. 74, no. 1, 2017, Art. no. 012010.

[40] H. McGowan and A. Clark, "Identification of dust transport pathways from Lake Eyre, Australia using Hysplit," *Atmos. Environ.*, vol. 42, no. 29, pp. 6915–6925, 2008.

[41] T. Chai, A. Crawford, B. Stunder, M. J. Pavolonis, R. Draxler, and A. Stein, "Improving volcanic ash predictions with the HYSPLIT dispersion model by assimilating MODIS satellite retrievals," *Atmos. Chem. Phys.*, vol. 17, no. 4, pp. 2865–2879, 2017.

[42] E. K. Smith and S. Weintraub, "The constants in the equation for atmospheric refractive index at radio frequencies," *Proc. IRE*, vol. 41, no. 8, pp. 1035–1037, 1953.

[43] T. Ozawa, E. Fujita, and H. Ueda, "Crustal deformation associated with the 2016 Kumamoto Earthquake and its effect on the magma system of Aso volcano," *Earth, Planets Space*, vol. 68, no. 1, pp. 1–15, 2016.

[44] M. Bevis, S. Businger, T. A. Herring, C. Rocken, R. A. Anthes, and R. H. Ware, "GPS meteorology: Remote sensing of atmospheric water vapor using the global positioning system," *J. Geophys. Res. Atmos.*, vol. 97, no. D14, pp. 15787–15801, 1992.

[45] M. Bevis et al., "GPS meteorology: Mapping zenith wet delays onto precipitable water," *J. Appl. Meteorol. Climatol.*, vol. 33, no. 3, pp. 379–386, 1994.

[46] C. Yu, *Generic Interferometric Synthetic Aperture Radar Atmospheric Correction Model and Its Application to Co-And Post-Seismic Motions*, Newcastle, U.K.: Newcastle Univ., 2019.

[47] H. Berrada Baby, P. Gole, and J. Lavergnat, "A model for the tropospheric excess path length of radio waves from surface meteorological measurements," *Radio Sci.*, vol. 23, no. 6, pp. 1023–1038, 1988.

[48] S. N. Sailellah and Y. Fukushima, "Comparison of tropospheric delay correction methods for InSAR analysis using a mesoscale meteorological model: A case study from Japan," *Earth, Planets Space*, vol. 75, no. 1, pp. 1–15, 2023.

[49] C. Yu, Z. Li, and N. T. Penna, "Interferometric synthetic aperture radar atmospheric correction using a GPS-based iterative tropospheric decomposition model," *Remote Sens. Environ.*, vol. 204, pp. 109–121, 2018, doi: 10.1016/j.rse.2017.10.038.

[50] D. P. Dee et al., "The ERA-Interim reanalysis: Configuration and performance of the data assimilation system," *Quart. J. Roy. Meteor. Soc.*, vol. 137, no. 656, pp. 553–597, 2011.
[51] H. Hersbach et al., "The ERA5 global reanalysis," *Quart. J. Roy. Meteor. Soc.*, vol. 146, no. 730, pp. 1999–2049, 2020.
[52] R. Gelaro et al., "The modern-era retrospective analysis for research and applications, version 2 (MERRA-2)," *J. Climate*, vol. 30, no. 14, pp. 5419–5454, 2017.
[53] Y. Wang, L. Chang, W. Feng, S. Samsonov, and W. Zheng, "Topography-correlated atmospheric signal mitigation for InSAR applications in the Tibetan plateau based on global atmospheric models," *Int. J. Remote Sens.*, vol. 42, no. 11, pp. 4364–4382, 2021.
[54] B. Gao and Y. Kaufman, *MODIS Atmosphere L2 Water Vapor Product. NASA MODIS Adaptive Processing System*, vol. 4. Greenbelt, MD, USA: Goddard Space Flight Center, 2015.
[55] E. Borbas, P. Menzel, and B. Gao, *MODIS Atmosphere L2 Water Vapor Product. NASA MODIS Adaptive Processing System*. Greenbelt, MD, USA: Goddard Space Flight Center, 2017.
[56] P. Liu et al., "Resolving surface displacements in Shenzhen of China from time series InSAR," *Remote Sens.*, vol. 10, no. 7, 2018, Art. no. 1162.
[57] Z. Li, J.-P. Muller, and P. Cross, "Comparison of precipitable water vapor derived from radiosonde, GPS, and moderate-resolution imaging spectroradiometer measurements," *J. Geophys. Res. Atmos.*, vol. 108, no. D20, pp. 1–12, 2003, doi: 10.1029/2003JD003372.
[58] R. F. Hanssen, *Radar Interferometry: Data Interpretation and Error Analysis* (ser. Remote Sensing and Digital Image Processing). Norwell, MA, USA: Kluwer, 2001, p. 298.
[59] R. F. Hanssen, "Atmospheric heterogeneities from ERS tandem SAR interferometry and sea surface images," in *Proc. CEOS SAR Workshop*, 1998, pp. 3–6.
[60] J. L. Davis, G. Elgered, A. E. Niell, and C. E. Kuehn, "Ground-based measurement of gradients in the 'wet' radio refractivity of air," *Radio Sci.*, vol. 28, no. 6, pp. 1003–1018, 1993.
[61] K. Yang et al., "China meteorological forcing dataset (1979-2018)," National Tibetan Plateau / Third Pole Environment Data Center, 2019. [Online]. Available: https://doi.org/10.11888/AtmosphericPhysics.tpe.249369.file
[62] J. He et al., "The first high-resolution meteorological forcing dataset for land process studies over China," *Sci. Data.*, vol. 7, no. 1, pp. 1–11, 2020.
[63] K. Akiyama, H. Itoh, H. Masuda, S. Kasho, and T. Sakamoto, "Operational validation of precise orbit determination for ALOS-2," in *Proc. 14th Int. Conf. Space Oper.*, 2016, Art. no. 2521.

Peng Liu received the B.Eng. degree in surveying and mapping from Central South University, Changsha, China, in 2008, and the Ph.D. degree in space geodesy from the University of Glasgow, Glasgow, U.K., in 2013.

He is currently a Research Assistant Professor with the Department of Earth and Space Sciences, Southern University of Science and Technology, Shenzhen, China. His research interests include synthetic aperture radar interferometry and its applications in earth surface processes, e.g., land subsidence, landslides, building scale deformation, and other geohazards.

Xiaofei Chen received the Ph.D. degree in geophysics from the University of Southern California (USC), Los Angeles, CA, USA, in 1991.

He was a Research Associate with USC from 1992 to 1996. He was a Professor with Peking University, Beijing, China, from 1996 to 2008, and the University of Science and Technology of China, Hefei, China, from 2008 to 2016. In 2016, he joined the Southern University of Science and Technology, Shenzhen, China, as the Initiatory Departmental Head of Earth and Space Sciences. His research interests include theoretical and computational geophysics, seismology, and their applications in earthquake hazard mitigation and earth resource exploration.